

Supporting Information

for

Structural Characterization of a Polycrystalline Epitaxially-Fused Colloidal Quantum Dot Superlattice by Electron Tomography

Xiaolei Chu¹, Hamed Heidari², Alex Abelson², Davis Unruh³, Chase Hansen³, Caroline Qian⁴, Gergely Zimanyi², Matt Law^{3,4,5,*} and Adam. J. Moule^{1,*}

¹Department of Chemical Engineering, University of California, Davis, Davis, CA 95616, USA

² Department of Materials Science and Engineering, University of California, Irvine, Irvine, CA 92697, USA

³ Department of Physics, University of California, Davis, Davis, CA 95616, USA

⁴Department of Chemical and Biomolecular Engineering, University of California, Irvine, Irvine, CA 92697, USA

⁵Department of Chemistry, University of California, Irvine, Irvine, CA 92697, USA

***E-mail:** amoule@ucdavis.edu, matt.law@uci.edu

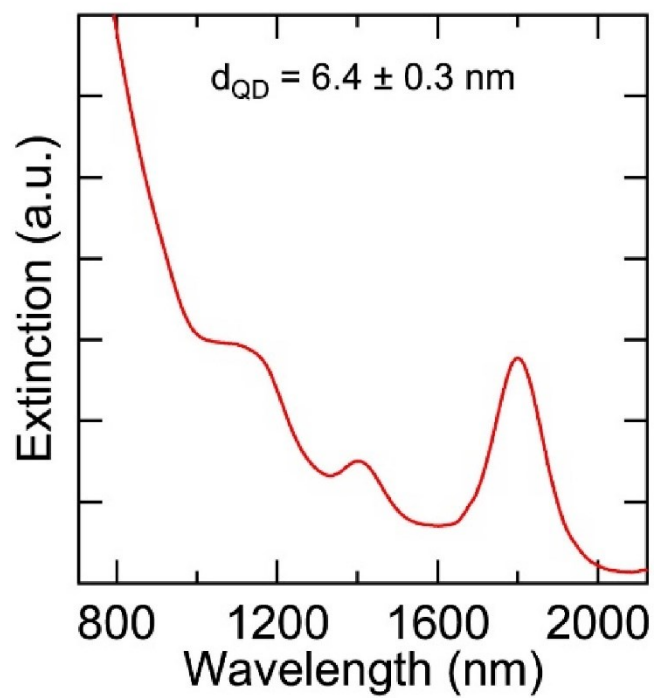


Figure S1. UV-vis extinction spectrum of colloidal PbSe QDs dispersed in tetrachloroethylene. The average QD diameter (6.4 nm) and standard deviation (0.3 nm) was determined using the empirical relationship by Moreels et al.¹

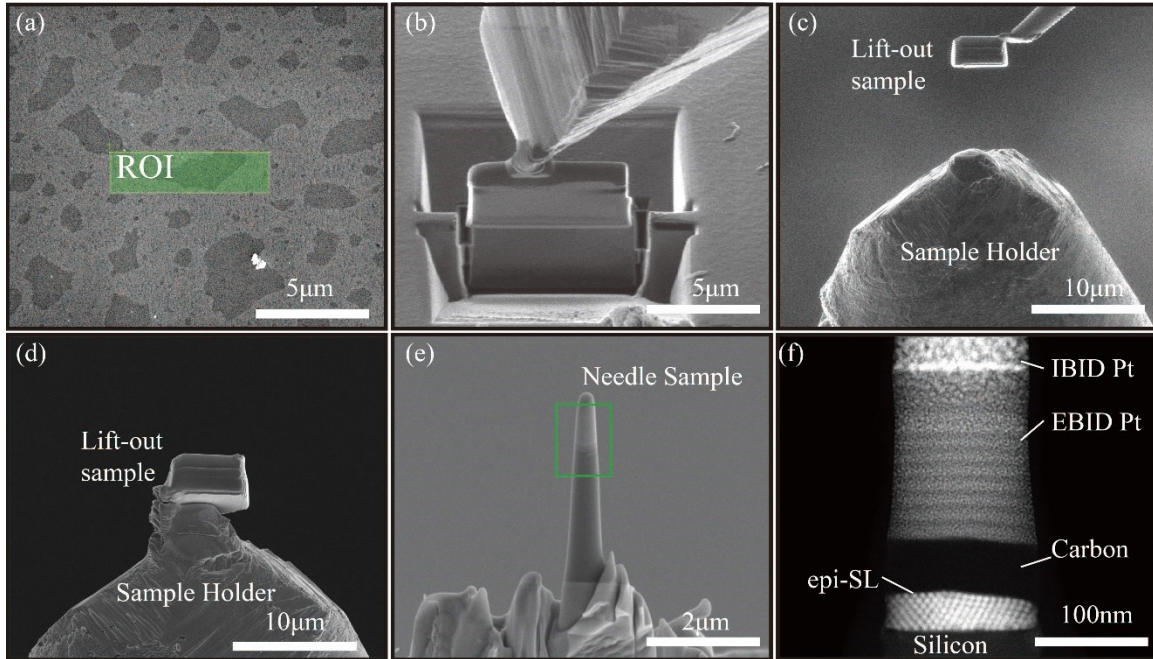


Figure S2. Steps of FIB tomography needle preparation. (a) The region of interest (ROI) is selected. (b) After carbon and platinum deposition, a wedge is FIB milled and attached to a lift-out probe by ion beam welding. (c) The wedge is transferred to the tip of a sample holder for needle tomography samples. (d-e) The wedge is FIB milled into a needle shape. (f) HAADF-STEM image of the finished needle, with layers labeled.²⁻⁴

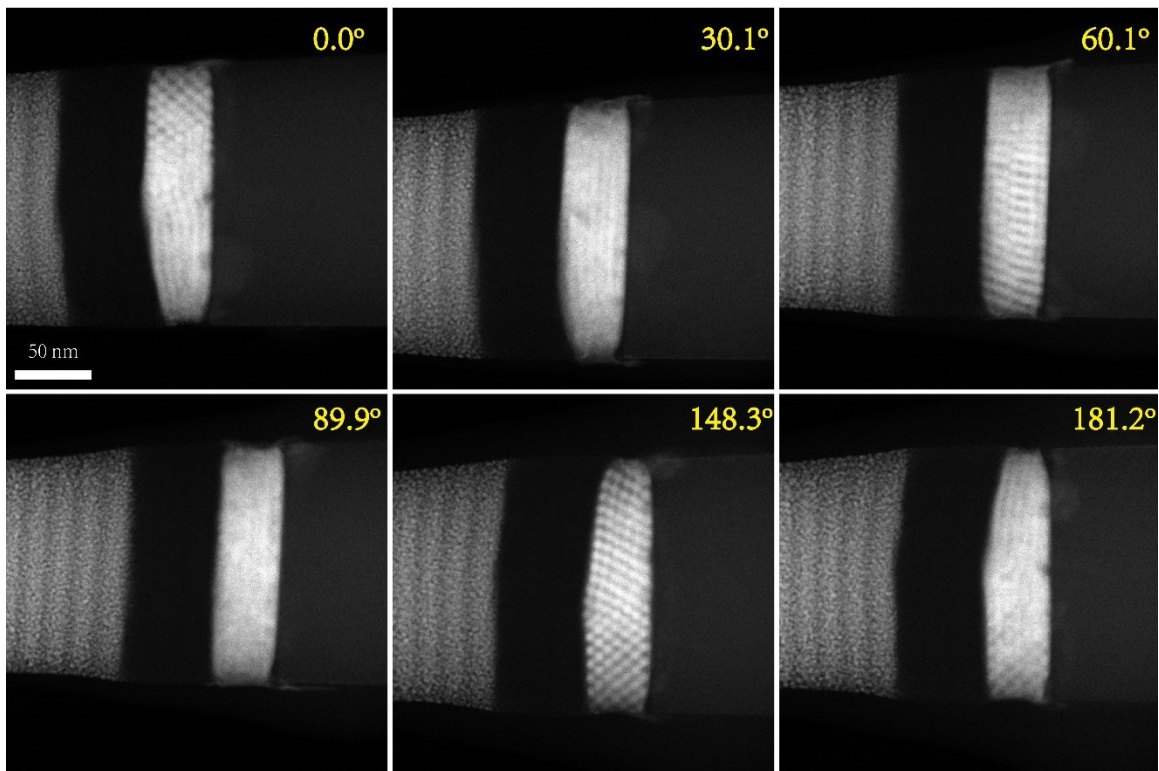


Figure S3. Six of the 181 images of the HAADF-STEM tilt-series, with tilt angles labeled.

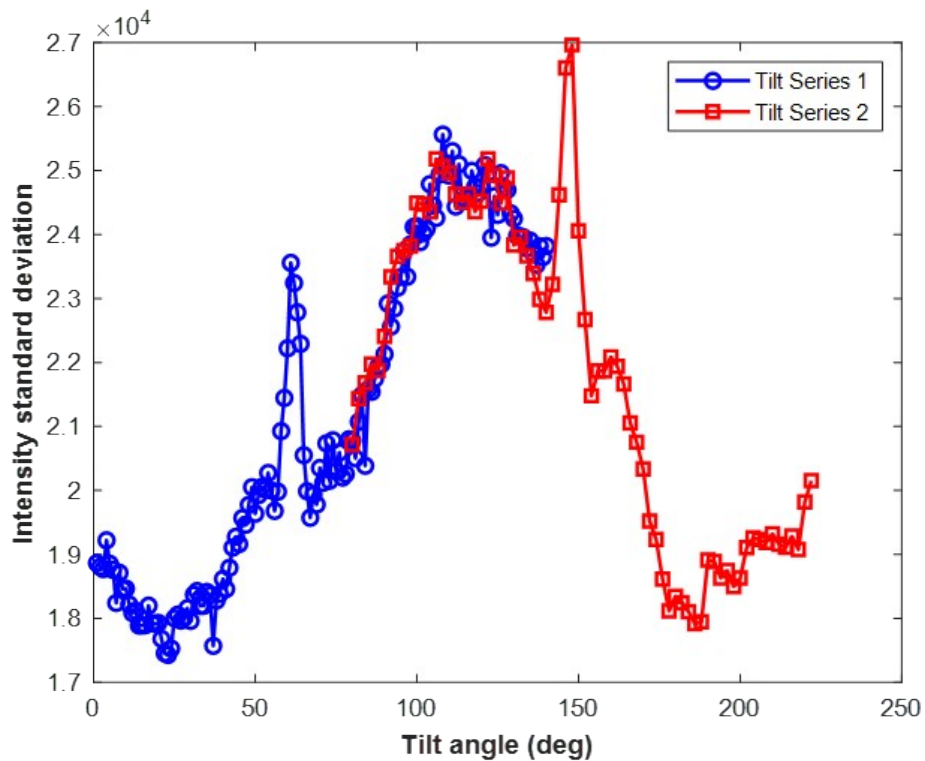


Figure S4. The entire projection tilt series set is obtained by merging two separately acquired tilt series. Since the ex-situ rotation angle of the holder is not precisely controlled, there is a redundant portion in tilt series 2 that repeats some of the tilt angles that are already sampled in tilt series 1. This overlapped portion is determined by monitoring the standard deviation of the intensity distribution of each image. This value varies as the sample is projected at different tilt angles. The overlapped portion is removed from series 2 and the non-redundant images are attached after series 1 to make the whole tilt series for tomographic reconstruction. The two sharp peaks occur at tilt angles for which the SL axes are inadvertently aligned along the electron beam direction.

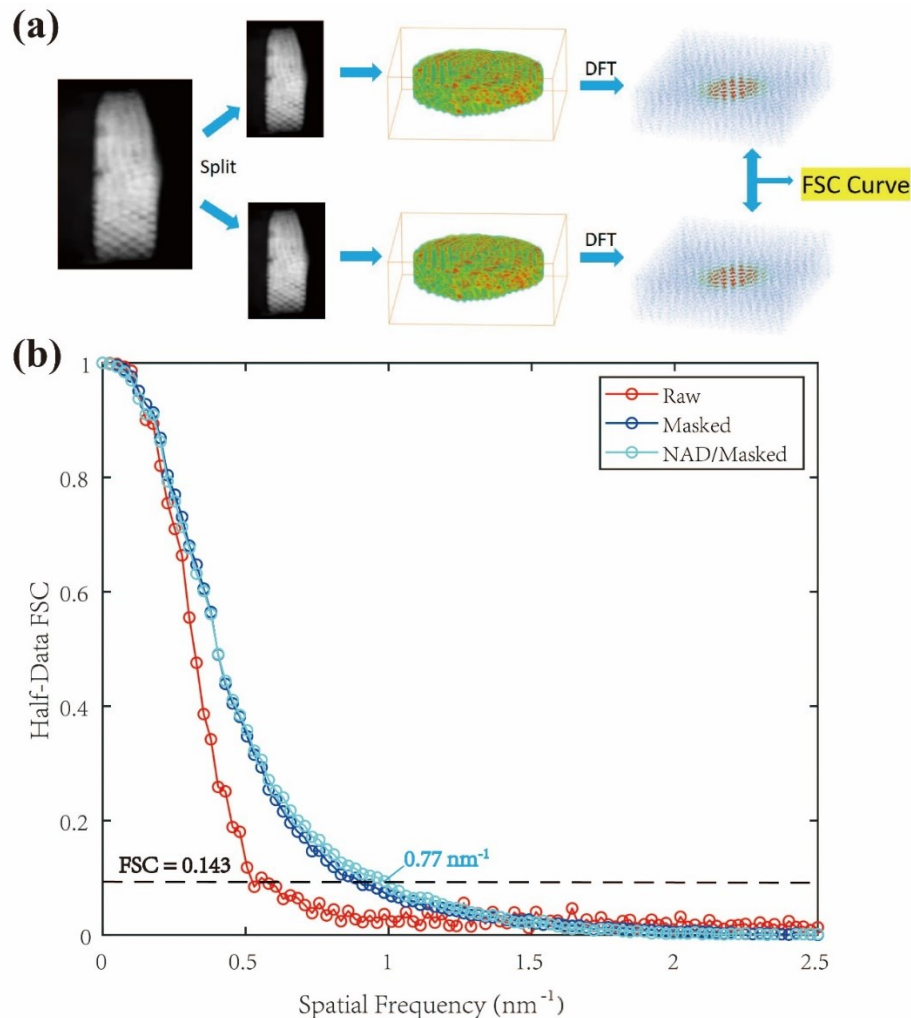


Figure S5. (a) To conduct Fourier Shell Correlation, the 2D projection images are split into two subsets, with odd-indexed images in one set and even-indexed images in the other. This is to ensure that both subsets are mutually exclusive but still cover the entire tilt angle range. The halves are independently aligned and reconstructed using SIRT and the spatial frequency information is extracted through 3D Discrete Fourier Transformation of the half reconstructions for evaluating correlation.⁴ (b) Fourier Shell Correlation data between the two reconstructed halves as illustrated in Fig. S5a. In the “masked” data, the voxel intensity is set to zero if it is $\geq 2\sigma$ from the mean of the Gaussian-fit intensity distribution of the QDs in the reconstruction. The FSC threshold value is selected to be 0.143.⁶ When the correlation is above the threshold, the orthogonal reconstructions share common structural features that stand out from random noise at the corresponding spatial frequency $f_c = 0.77 \text{ nm}^{-1}$. Thus the resolution of the half reconstruction is $r_c = 1/f_c = 1.3 \text{ nm}$. The other set was reconstructed using the non-linear anisotropic diffusion filter and does not exhibit significant decrease of the resolution. The resolution of the full data set with both odd and even indexed images evaluated to be $r_c = 1/(2f_c) = 0.65 \text{ nm}$.⁵

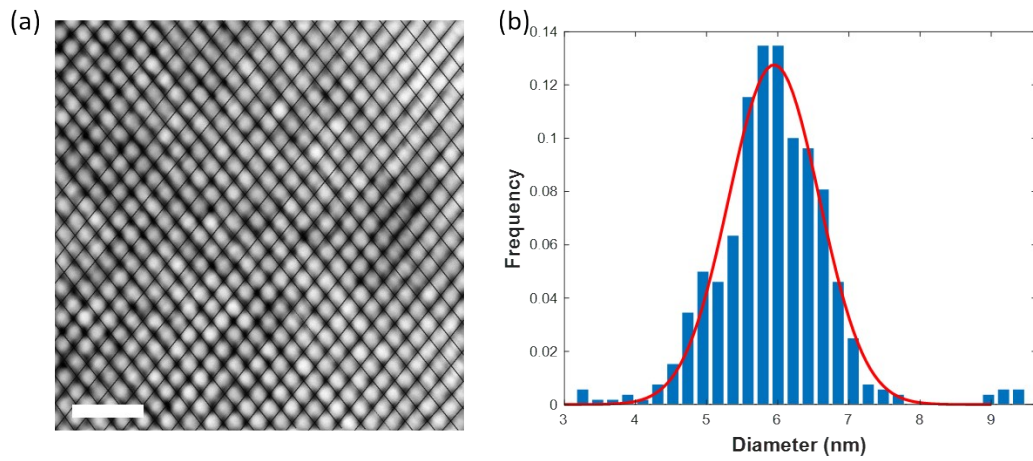


Figure S6. The diameter of the QDs is determined by analyzing conventional STEM images of the SLs. (a) A program is used to isolate each QD from its connected neighbors and calculate the effective diameter of the dot. The scale bar is 20 nm. (b) The result of QD size distribution from image analysis. The red line is a Gaussian fit to the histogram.

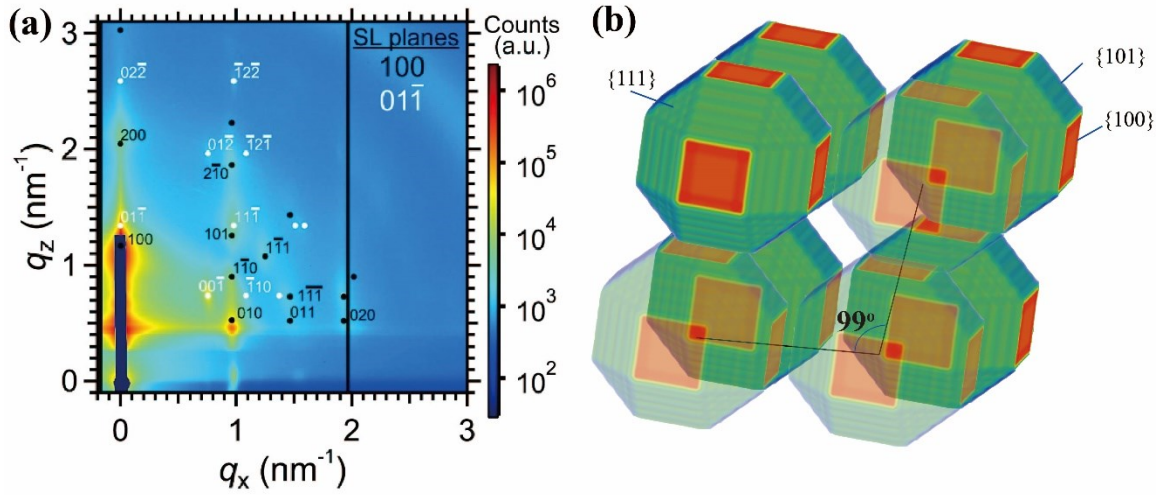


Figure S7. (a) Grazing incidence small-angle X-ray scattering pattern of the film used in this study, overlaid with calculated diffraction patterns from (100)- and (011̄)-oriented epi-SL planes (the most prominent SL orientations) with SL unit cell lattice parameters $a = 6.6$ nm and $\alpha = 99^\circ$. (b) Model of the epi-SL showing fusion along PbSe{100}. Additional details of the structure can be found in **Ref 6**.

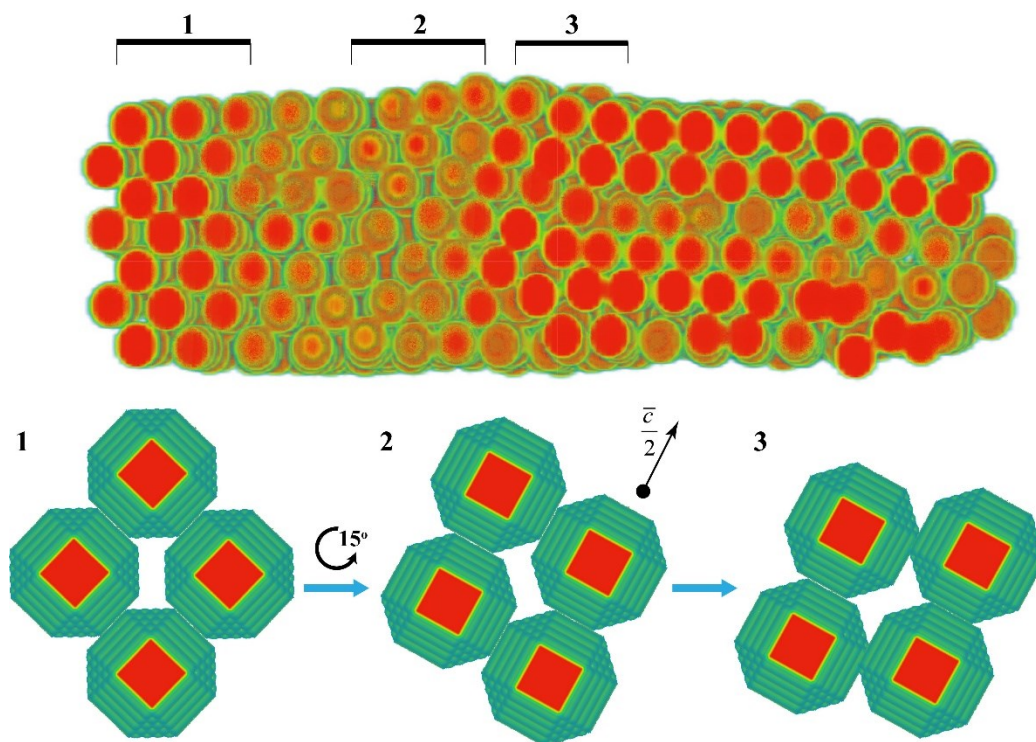


Figure S8. Proposed mechanism for SL structure transition from grain II to grain I. The SL structure in the far left end (region 1) undergoes a slight tilt of 15 degrees from near-perfect $(011)_{\text{SL}}$ orientation as the structure propagates to the right into region 2. A glide of $(100)_{\text{SL}}$ plane occurs in between region 2 and 3 that can be effectively considered as if the orientation of SL changes 90 degrees counter-clockwise. Such process may potentially also alter the β angle, explaining our statistics shown in Table 1.

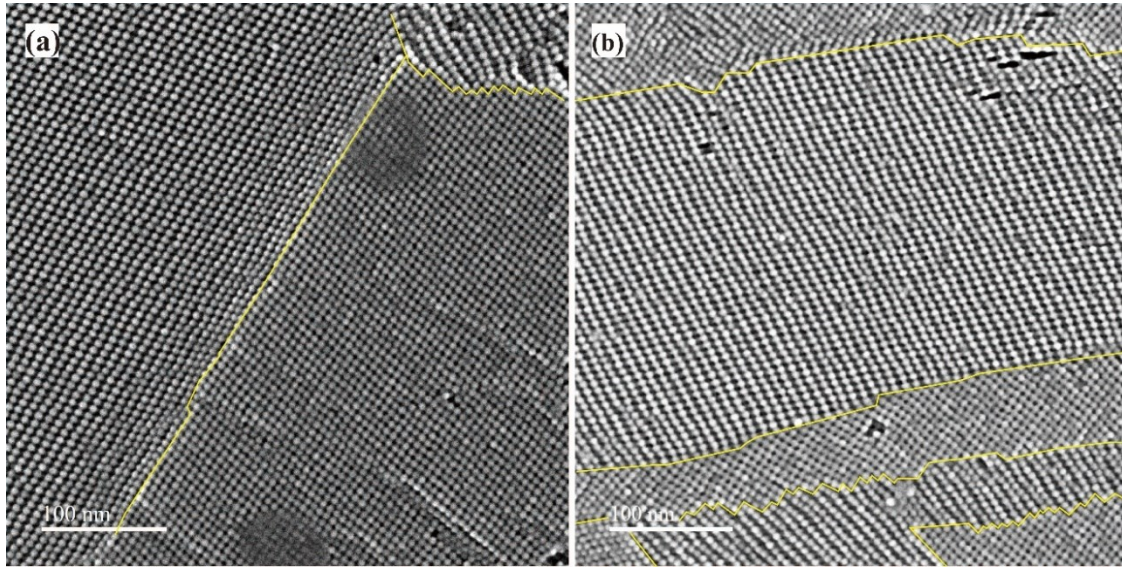


Figure S9. Plan-view SEM images of grain boundaries of the SL sample, showing the structure of these GBs. (a) A tricrystalline region that is similar to the tomography sample. (b) Corrugated grain boundaries between $(100)_{\text{SL}}$ -oriented and $(01\bar{1})_{\text{SL}}$ -oriented grains. Scale bars are 100 nm.

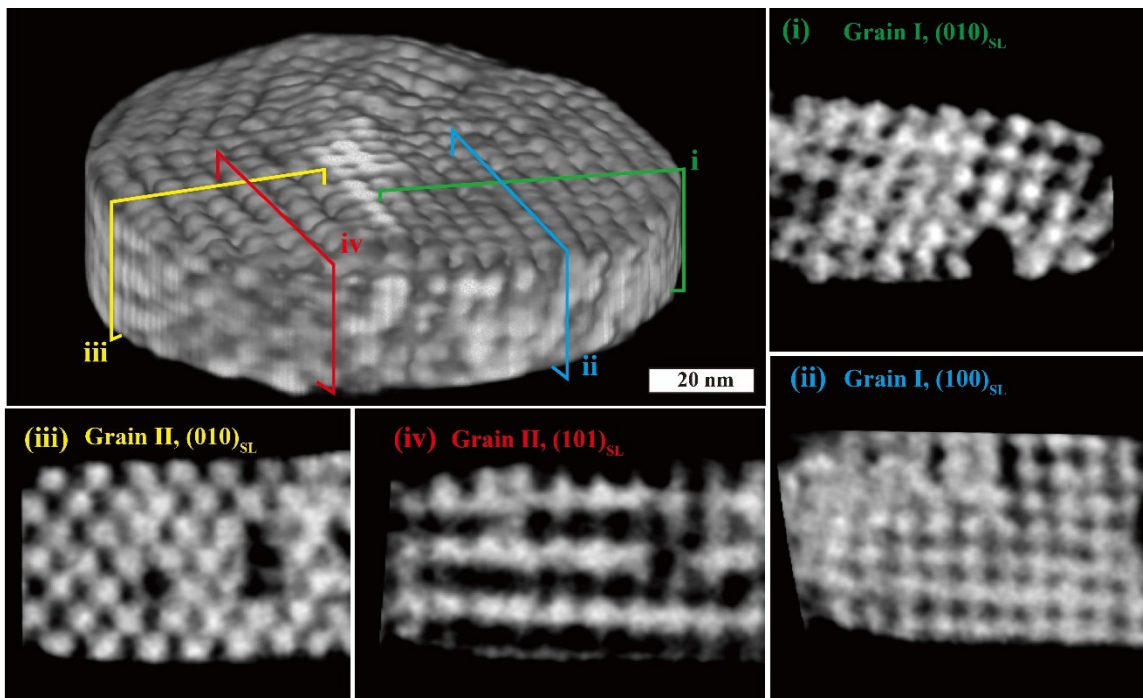


Figure S10. Regional slices of the tomogram showing arrangements of the QDs and the necks in grain I (i,ii) and II (iii,iv). The bisecting planes are annotated as plane (i-iv) which indicated the position of the respective slices and also represent different lattice planes indexed in the corresponding small panels for different grains. Plane (i) and (iii) are parallel to each other, as well as plane (ii) and (iv). All panels share the same scale bar.

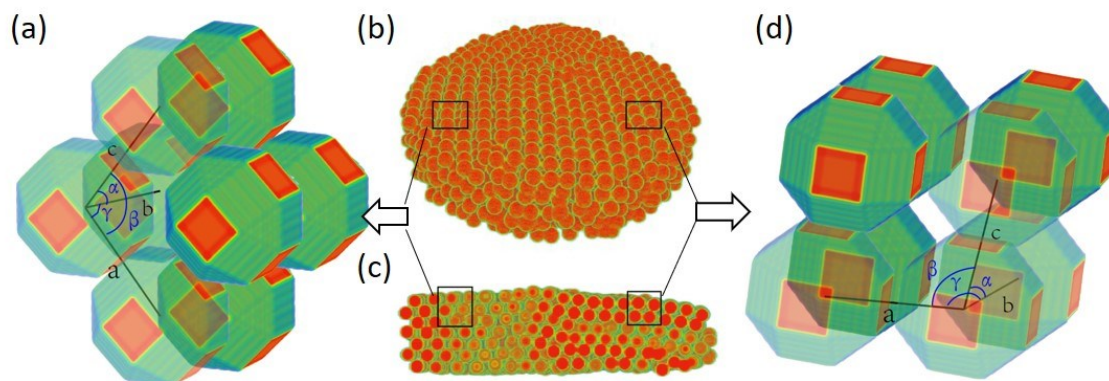


Figure S11. The epi-SL can be reconstructed with QDs represented by spheres of identical size positioned according to the CoM data. (b) Perspective and (c) cross-sectional views of the sample with the QDs represented by perfect spheres. (a,d) Labeling conventions for assigning lattice parameters to grain I and II, respectively. Red planes correspond to the $\{100\}$ facets.

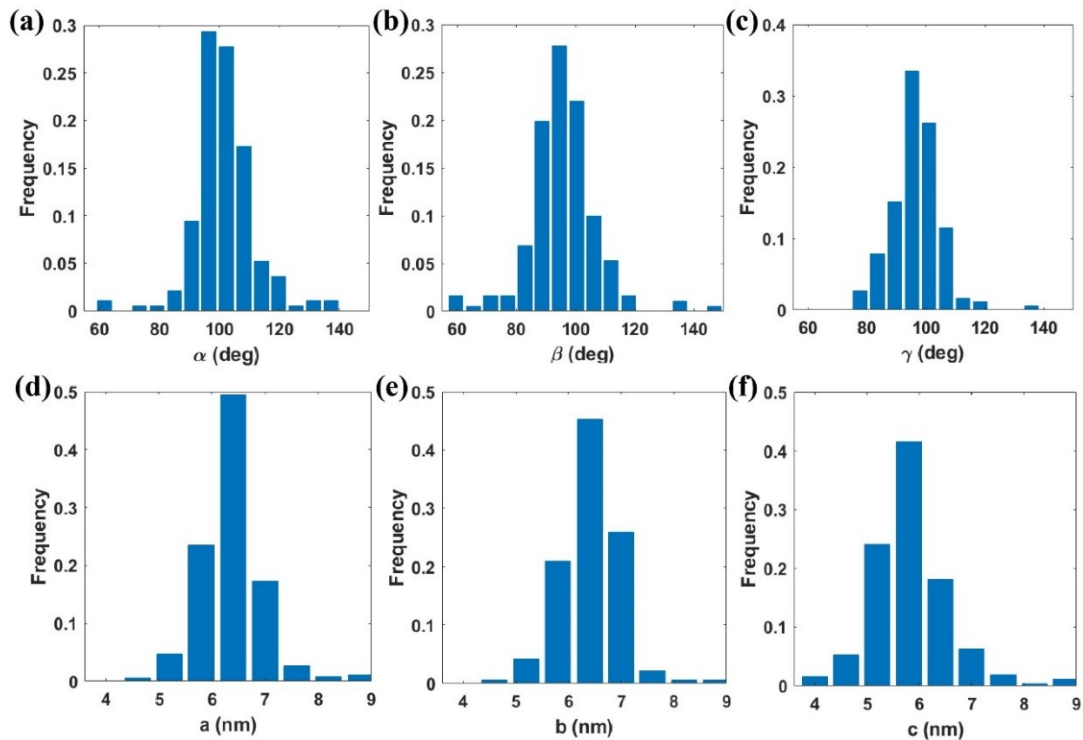


Figure S12. Histograms of SL lattice parameters in grain I, including (a-c) lattice angles α , β and γ , and (d-f) lattice spacing a , b and c .

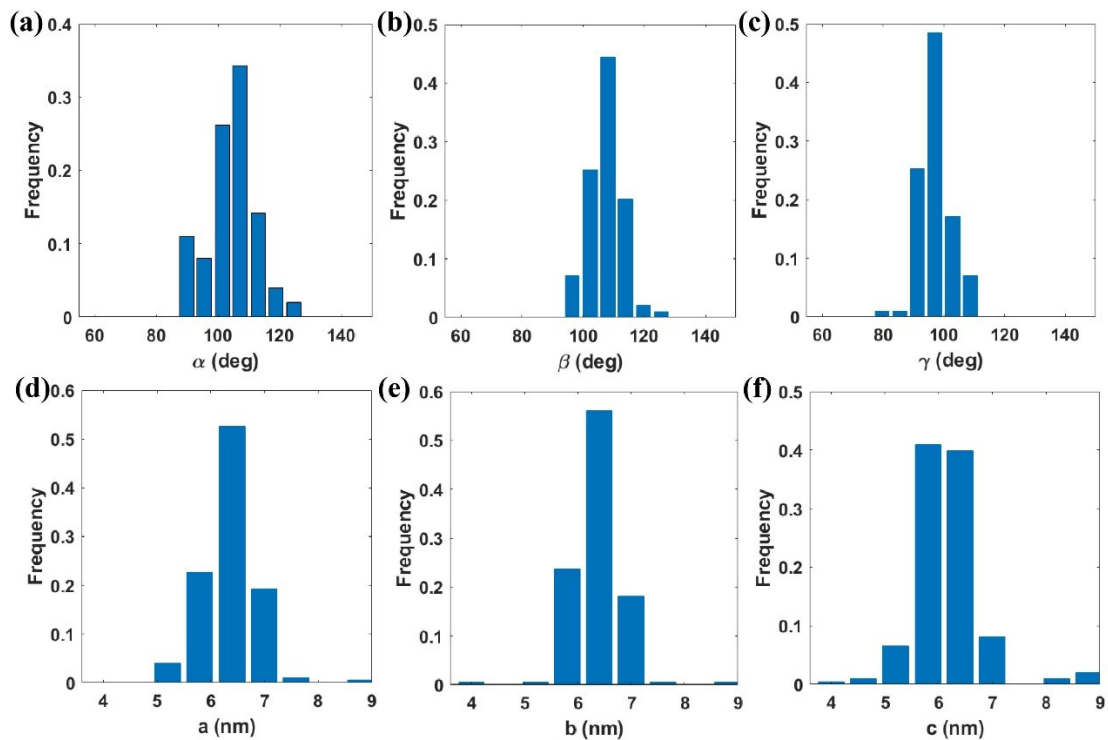


Figure S13. Histograms of SL lattice parameters in grain II, including (a-c) lattice angles α , β and γ , and (d-f) lattice spacing a , b and c .

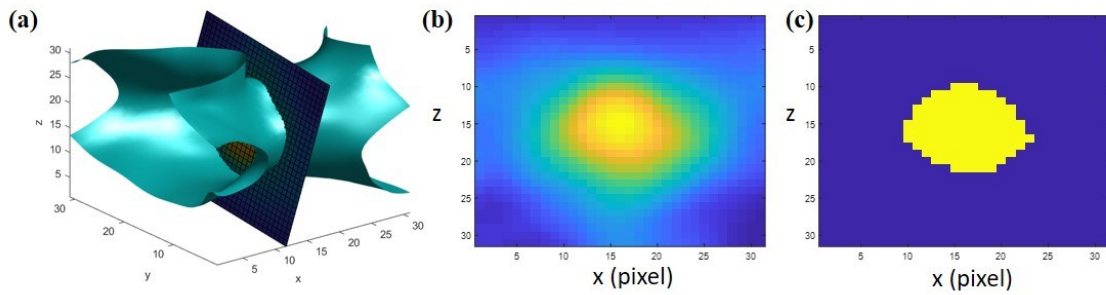


Figure S14. An illustration of how the neck diameter is determined. In (a), two necked QDs are shown in iso-surface form. A plane is generated such that it is perpendicular to the vector between the centers of mass of the necked QDs. This plane is then allowed to slide along this vector to locate the minimum area of the neck. (b) Image of this plane at the neck minimum. Using a threshold value (the same value for the masking reconstruction in Fig. S5), (b) is reduced to (c) to estimate the neck shape and area. The neck diameter is calculated as the effective diameter of the neck area.

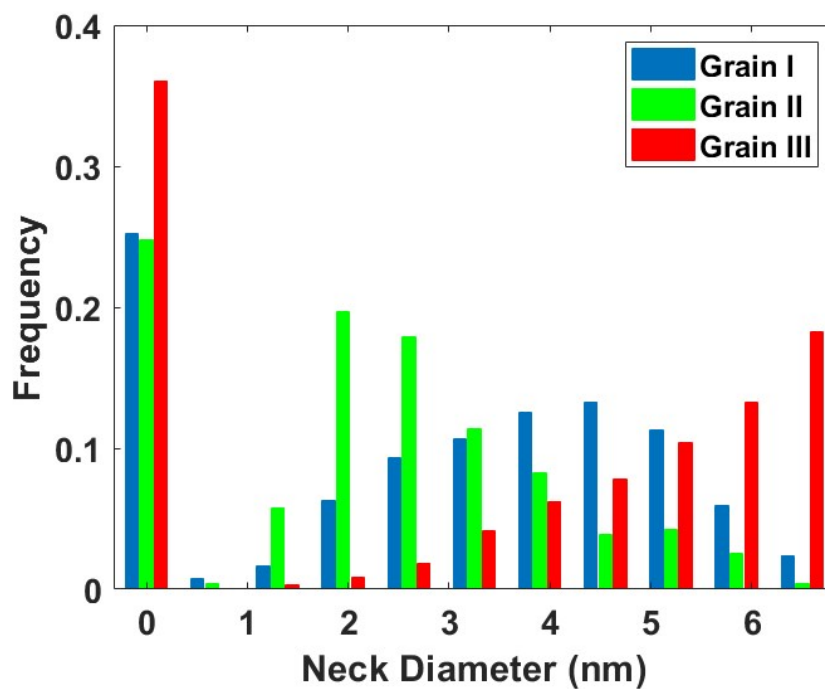


Figure S15. Histograms of diameters of each individual neck characterized from each of the three grains. Zero diameter represents a “missing neck”.

Neck number heat maps

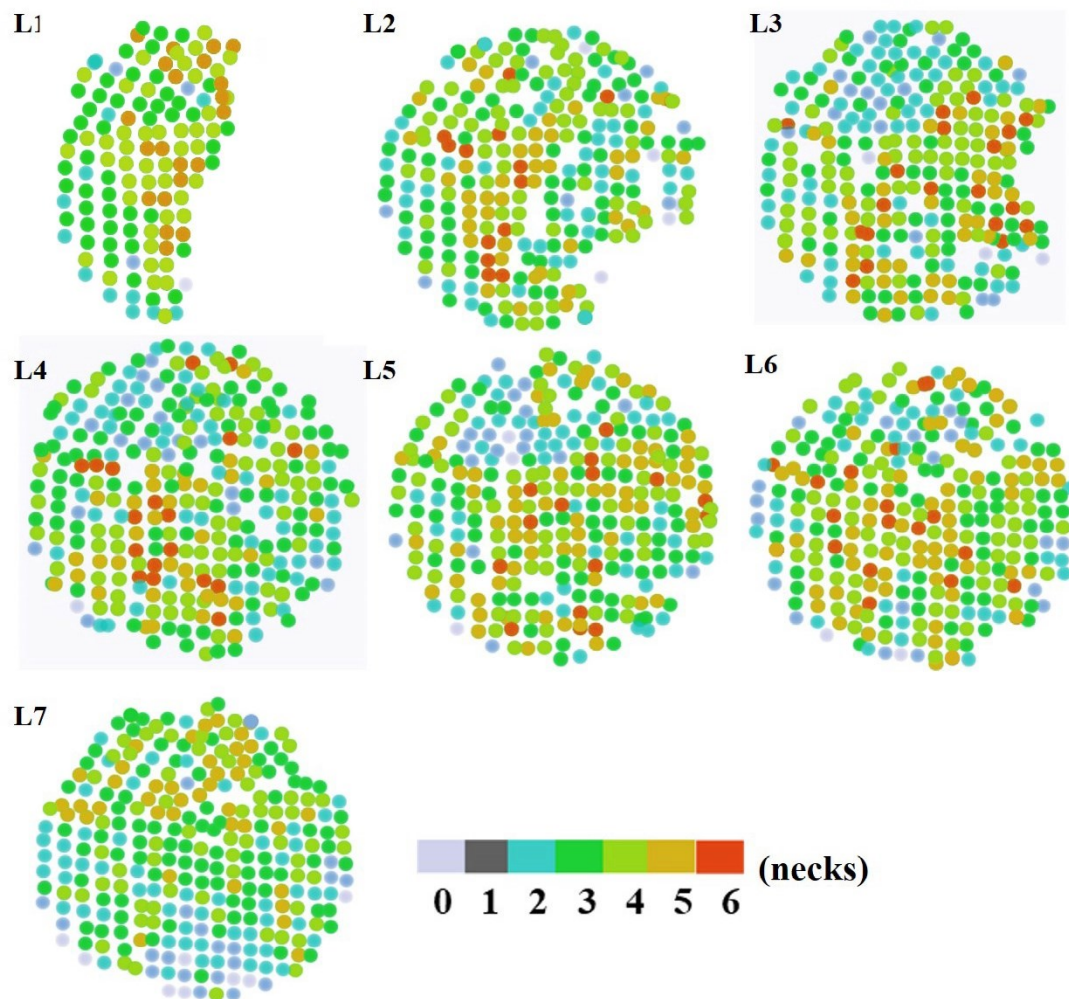


Figure S16. Heat maps of the neck number for each QD in the sample. Each circle represents a QD in L1-7.

Neck diameter heat maps

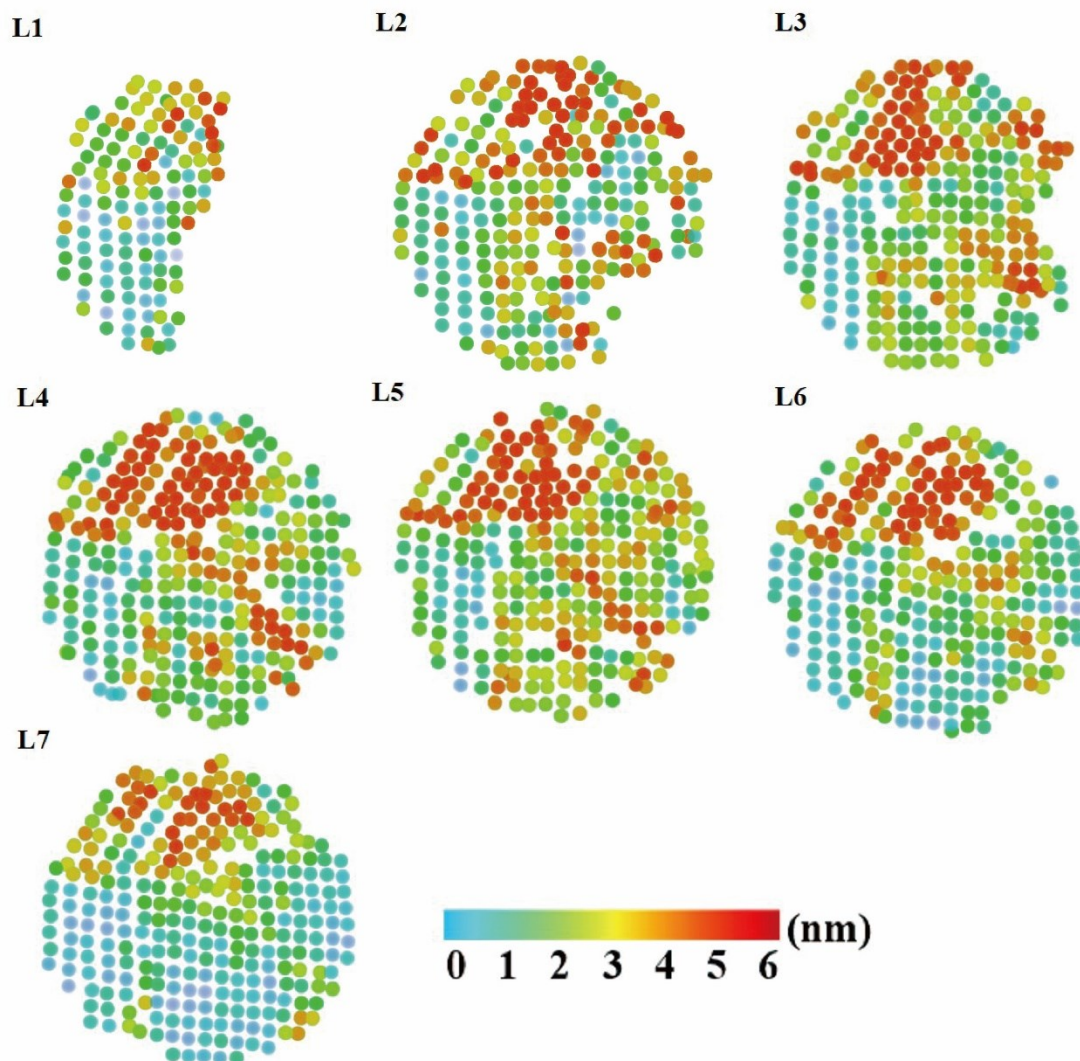


Figure S17. Heat maps of the average neck diameter for each QD in the sample. Each circle represents a QD in L1-7.

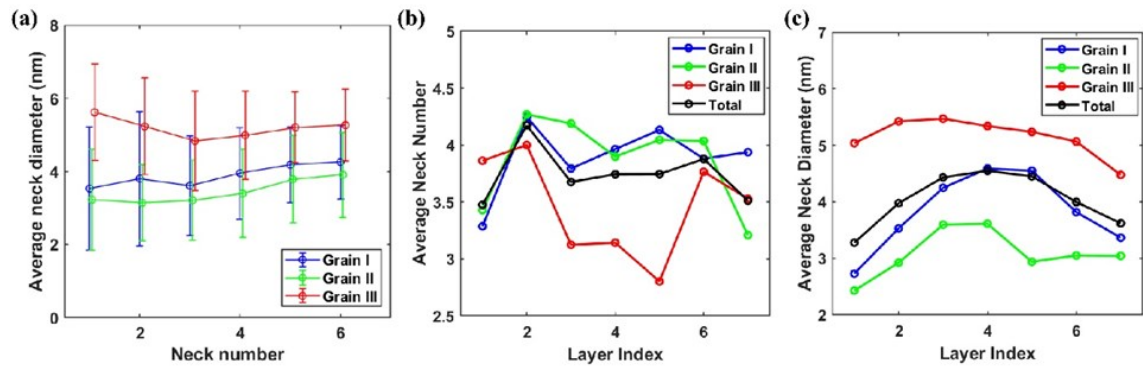


Figure S18. (a) Average neck diameter as a function of neck number for each QD in grains I, II, and III. Error bars denote one standard deviation. (b) Average neck number for each QD layer in the tomogram. Layer 1 is the top of the epi-SL (QD/gas interface) and Layer 7 is the bottom of the epi-SL (QD/liquid interface). (c) Average neck diameter for each QD layer.

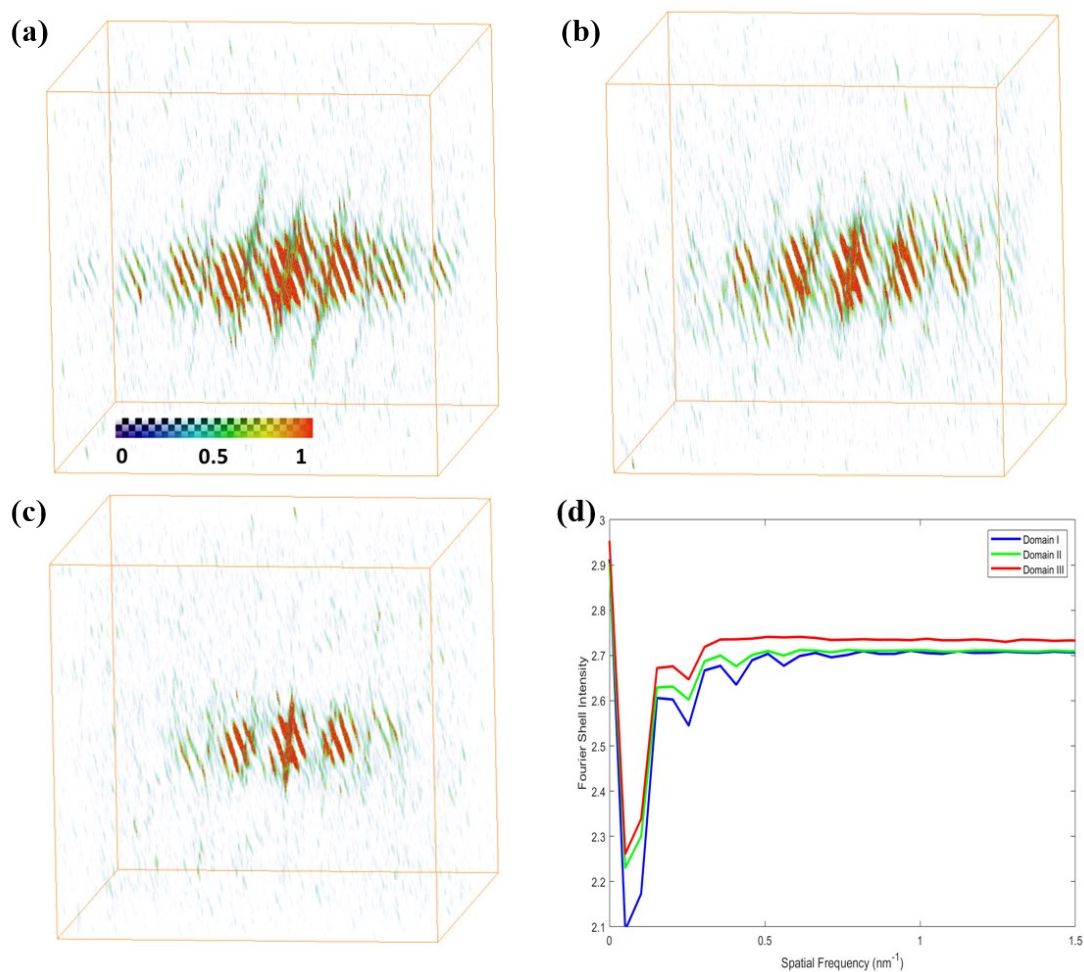


Figure S19. (a-c) Separate 3D Fourier transformations of (a) grain I, (b) grain II and (c) grain III. (d) Fourier Shell Intensity comparison between the three grains. Both grain I and grain II show structural features at high spatial frequency, while grain III lacks fine feature at sub-QD length scales (<6 nm).

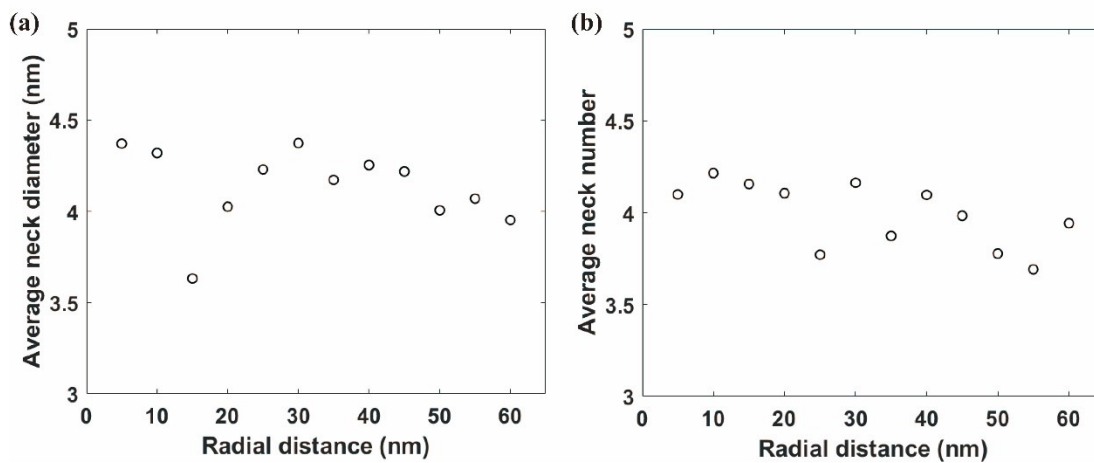


Figure S20. Radial distribution of (a) average neck diameter and (b) average neck number.

References

1. Moreels, I.; Lambert, K.; De Muynck, D.; Vanhaecke, F.; Poelman, D.; Martins, J.C.; Allan, G.; Hens, Z. Composition and Size-Dependent Extinction Coefficient of Colloidal PbSe Quantum Dots. *Chem. Mater.* **2007**, *19*, 6101-6106.
2. Dkhil, S. B.; Pfannmöller, M.; Saba, M. I.; Gaceur, M.; Heidari, H.; Vidélot-Ackermann, C.; Margeat, O.; Guerrero, A.; Bisquert, J.; Garcia-Belmonte, G.; Mattoni, A. Toward High-Temperature Stability of PTB7-Based Bulk Heterojunction Solar Cells: Impact of Fullerene Size and Solvent Additive. *Adv. Energy Mater.* **2017**, *7*, 1601486.
3. Langford, R. M.; Clinton, C. In Situ Lift-Out Using a FIB-SEM System. *Micron* **2004**, *35*, 607-611.
4. Miller, M. K.; Russell, K. F.; Thompson, G. B. Strategies for Fabricating Atom Probe Specimens with a Dual Beam FIB. *Ultramicroscopy* **2005**, *102*, 287-298.
5. Frank J. *Electron tomography*. Springer: New York; London: Plenum **1992**; pp 399.
6. Grigorieff, N.; Harrison, S. C. Near-Atomic Resolution Reconstructions of Icosahedral Viruses from Electron Cryo-Microscopy. *Curr. Opin. Struct. Biol.* **2011**, *21*, 265-273.
7. Abelson, A.; Qian, C.; Salk, T.; Luan, Z.; Fu, K.; Zheng, J.-G.; Wardini, J. L.; Law, M. Collective Topo-Epitaxy in the Self-assembly of a 3D Quantum Dot Superlattice. *Nat. Mater.* **2020**, *19*, 49-55.